The Astrophysical Journal, 913:3 (12pp), 2021 May 20 https://doi.org/10.3847/1538-4357/abf24a

The Cepheid Distance to the Narrow-line Seyfert 1 Galaxy NGC 4051

W. Yuan[1], L. M. Macri[2], B. M. Peterson[3,4], A. G. Riess[1,5], M. M. Fausnaugh[3,6], S. L. Hoffmann[5], G. S. Anand[7], M. C. Bentz[8], E. Dalla Bontà[9,10], R. I. Davies[11], G. De Rosa[5], L. Ferrarese[12], C. J. Grier[3,13], E. K. S. Hicks[14], C. A. Onken[15,16], R. W. Pogge[3,4], T. Storchi-Bergmann[17], and M. Vestergaard[13,18]
[1] Department of Physics & Astronomy, Johns Hopkins University, Baltimore, MD 21218, USA
[2] George P. and Cynthia W. Mitchell Institute for Fundamental Physics & Astronomy, Department of Physics & Astronomy, Texas A&M University, College Station, TX 77843, USA
[3] Department of Astronomy, The Ohio State University, 140 W 18th Avenue, Columbus, OH 43210, USA
[4] Center for Cosmology and AstroParticle Physics, The Ohio State University, 191 West Woodruff Avenue, Columbus, OH 43210, USA
[5] Space Telescope Science Institute, 3700 San Martin Drive, Baltimore, MD 21218, USA
[6] Kavli Institute for Space and Astrophysics Research, Massachusetts Institute of Technology, 77 Massachusetts Avenue, Cambridge, MA 02139, USA
[7] Institute for Astronomy, University of Hawaii, 2680 Woodlawn Drive, Honolulu, HI 96822, USA
[8] Department of Physics and Astronomy, Georgia State University, 25 Park Place, Suite 605, Atlanta, GA 30303, USA
[9] Dipartimento di Fisica e Astronomia "G. Galilei,"Università di Padova, Vicolo dell'Osservatorio 3, I-35122 Padova, Italy
[10] INAF-Osservatorio Astronomico di Padova, Vicolo dell'Osservatorio 5 I-35122, Padova, Italy
[11] Max Planck Institut für extraterrestrische Physik, Postfach 1312, D-85741, Garching, Germany
[12] NRC Herzberg Astronomy and Astrophysics, National Research Council, 5071 West Saanich Road, Victoria, BC V9E 2E7, Canada
[13] Steward Observatory, University of Arizona, 933 North Cherry Avenue, Tucson, AZ 85721, USA
[14] Department of Physics and Astronomy, University of Alaska Anchorage, AK 99508, USA
[15] Research School of Astronomy and Astrophysics, Australian National University, Canberra, ACT 2611, Australia
[16] Australian Research Council (ARC) Centre of Excellence for All-sky Astrophysics (CAASTRO), Australia
[17] Departamento de Astronomia, Universidade Federal do Rio Grande do Sul, Av. Bento Goncalves 9500, 91501 Porto Alegre, RS, Brazil
[18] DARK Niels Bohr Institute, University of Copenhagen, Jagtvej 128, DK-2200 Copenhagen N, Denmark
Received 2020 December 10; revised 2021 March 24; accepted 2021 March 24; published 2021 May 18

Abstract

We derive a distance of $D = 16.6 \pm 0.3$ Mpc ($\mu = 31.10 \pm 0.04$ mag) to the archetypal narrow-line Seyfert 1 galaxy NGC 4051 based on Cepheid period–luminosity relations and new Hubble Space Telescope multiband imaging. We identify 419 Cepheid candidates and estimate the distance at both optical and near-infrared wavelengths using subsamples of precisely photometered variables (123 and 47 in the optical and near-infrared subsamples, respectively). We compare our independent photometric procedures and distance-estimation methods to those used by the Supernovae, H0, for the Equation of State team and find agreement to 0.01 mag. The distance we obtain suggests an Eddington ratio of $\dot{m} \approx 0.2$ for NGC 4051, typical of narrow-line Seyfert 1 galaxies, unlike the seemingly odd value implied by previous distance estimates. We derive a peculiar velocity of -490 ± 34 km s^{-1} for NGC 4051, consistent with the overall motion of the Ursa Major Cluster in which it resides. We also revisit the energetics of the NGC 4051 nucleus, including its outflow and mass accretion rates.

Unified Astronomy Thesaurus concepts: Cepheid variable stars (2106); Distance measure (395); Cepheid distance (217); AGN host galaxies (2017); Hubble Space Telescope (761); HST photometry (756); Time series analysis (1916); Near infrared astronomy (1093); Distance indicators (394); Galaxy distances (590)

Supporting material: machine-readable tables, tar.gz file, interactive figure

1. Introduction

The distance to an astronomical object is one of the most fundamental measurements that can be made, and yet it is also one of the most difficult. Without an accurate distance, measurements of many other parameters are of limited utility. In the case of the nearest active galactic nuclei (AGNs), the lack of accurate and precise distance measurements to these objects precludes a robust calibration of their physical properties, even though, compared to the general AGN population, their detailed structure is best resolved and their dynamics and energetics are the most easily studied. Thus, obtaining accurate distances is the most urgent priority toward achieving an accurate physical description of the accretion, feedback, and energetics of nearby AGNs.

NGC 4051, one of the original six Seyfert galaxies (Seyfert 1943) and one of the lowest-redshift AGNs ($z = 0.00234$), illustrates some of the difficulties. NGC 4051 is the archetype of the subclass of AGNs known as "narrow-line Seyfert 1 galaxies" (NLS1s; Osterbrock & Pogge 1985), which are thought to be high Eddington ratio objects; the Eddington ratio $\dot{m}$ is defined as the ratio of the mass accretion rate to the Eddington accretion rate, $\dot{m} = \dot{M}/\dot{M}_{\rm Edd}$. Since the accretion rate is $\dot{M} = L_{\rm bol}/\eta c^2$, where $L_{\rm bol}$ is the bolometric luminosity and η is the efficiency, as long as η is independent of $\dot{M}$, we can also write $\dot{m} = L_{\rm bol}/L_{\rm Edd}$, where $L_{\rm Edd}$ is the Eddington luminosity. To compute the bolometric luminosity, we must know the distance. Unfortunately, redshift-independent distances for NGC 4051 are ambiguous. Distances quoted in the literature cover a wide range, from a low of 8.8 Mpc (Sorce et al. 2014) to a high close to 18 Mpc (Wang et al. 2014; Yoshii et al. 2014). If NGC 4051 is at the lower end of this range, which is close to the redshift-based distance of 9.5 Mpc, its Eddington ratio is surprisingly low for an NLS1 galaxy. By using the bolometric correction and weighted mean mass and luminosity from Dalla Bontà et al. (2020), we find that at a distance of 9 Mpc the Eddington ratio would be $\dot{m} \approx 0.07$, which is fairly typical of other local Seyfert galaxies. However, if NGC 4051 is at the high end of this distance range, at 18 Mpc, $\dot{m} \approx 0.28$, which is more typical of NLS1s.

NGC 4051 is the first AGN for which strong evidence for inflows in molecular gas was found using near-infrared (NIR) integral-field spectroscopy (Riffel et al. 2008). The inferred geometry of the inflow depends strongly on the distance to the galaxy, taken to be 9.3 Mpc in that work. Similarly, X-ray spectra reveal a fast ionized outflow that loses kinetic energy by interaction with the interstellar medium in the host galaxy (Pounds 2014); the energetics and timescales again strongly depend on the distance to the AGN and are consequently systematically uncertain by a factor of several. Moreover, spatially resolved observations of the narrow-line region reveal a strong outflow component (Fischer et al. 2013), and again the energetics are uncertain on account of the poorly constrained distance. The quantitative results of these observations are important because they are probes of the feedback mechanisms through which supermassive black hole (SMBH) accretion can modify the interstellar medium and regulate star formation in the host galaxy. Understanding the physical mechanisms at work in both feeding and feedback, and determining whether or not the feedback mechanisms of theoretical models actually work in nature, requires detailed observations of the complex inner structure of AGNs. Nearby galaxies afford the only opportunity to test in detail, i.e., on sub-hundred pc scales, the prescriptions used in models of galaxy and SMBH coevolution. It is on scales of less than 100 pc that morphological differences between active and quiescent galaxies appear (Simões Lopes et al. 2007; García-Burillo & Combes 2012; Hicks et al. 2013; Davies et al. 2014). There is observational and theoretical evidence that disk processes are important in feeding AGNs across broad ranges of redshift and luminosity (e.g., Hopkins & Quataert 2010; Schawinski et al. 2012; Kocevski et al. 2012; Riffel et al. 2013; Schnorr-Müller et al. 2014; Storchi-Bergmann & Schnorr-Müller 2019), so what we learn about local AGNs is applicable to galaxies at $z > 1$, where coevolution largely occurs.

Finally, it is only in the nearest AGNs that we can compare SMBH masses measured from stellar or gas dynamical modeling, which are distance dependent, with those measured by reverberation mapping (RM), which are distance independent. NGC 4051 is challenging as the SMBH radius of influence ($r_{\rm BH} = GM/\sigma_*^2$, where M is the BH mass and σ_* is the stellar bulge velocity dispersion) is $\sim$0.67 pc; whether or not it is spatially resolvable with either the Hubble Space Telescope (HST) or the James Webb Space Telescope (JWST) is unclear given the factor of 2–3 uncertainty in the SMBH mass and the factor of 2 uncertainty in the distance, but it should nevertheless be possible to get at least meaningful constraints on the central mass with the integral-field unit on JWST.

Our goal is to eliminate distance-dependent ambiguities by determining a Cepheid-based distance to NGC 4051. The Cepheid period–luminosity relation (PLR) or Leavitt law (Leavitt & Pickering 1912) is a widely used empirical standard candle with a reach of at least $D \approx 40$ Mpc (Riess et al. 2016). It has been extensively applied to dozens of extragalactic systems, including the work of Bentz et al. (2019) and Yuan et al. (2020), hereafter Y20), who recently measured the Cepheid-based distances to the Seyfert 1 galaxies NGC 6814 and NGC 4151, respectively.

In this work, we derive a Cepheid distance to NGC 4051 using multiband HST observations. The rest of this paper is organized as follows. We present the observations, data reduction, and photometry in Section 2 and our Cepheid selection methods in Section 3. Our main result, the Cepheid distance to NGC 4051, is given in Section 4, and we discuss its implications in Section 5.

2. Observations, Data Reduction, and Photometry

We observed NGC 4051 and carried out the subsequent analysis following the same strategy used by Y20 for NGC 4151. We obtained optical and NIR HST images of a field that covers a large area of the disk (see Figure 1). We briefly summarize the observations, data reduction, and photometry procedure below and refer interested readers to Y20 for further details.

The NGC 4051 observations include 12, 3, 3, and 6 epochs in F350LP, F555W, F814W, and F160W, respectively. The observation baseline spans 73 days, during which the orientation angle of HST changed once. The observation log and exposure times are given in Table 1. We note that one of the two F555W images obtained in epoch 9 had a significantly worse FWHM, possibly due to increased jitter, and thus was excluded from further analysis.

We registered and drizzle combined all images using the `AstroDrizzle v2.2.6` package. We created master frames in each band by combining the respective images obtained in all epochs. We also created drizzled images of each F350LP epoch for variable detection. We modeled the surface brightness gradients across all images and subtracted them using the same methods as described by Y20.

We carried out point-spread function (PSF) photometry on the NGC 4051 images following identical procedures to those used in the case of NGC 4151 (Y20). We first derived a source list through a two-pass source detection on the F350LP master frame using `DAOPHOT/ALLSTAR` (Stetson 1987), then performed `ALLFRAME` (Stetson 1994) time-series photometry on the 12 epochs of images obtained through that filter. The frame-to-frame magnitude offsets were calculated based on 69 carefully selected secondary standards, which are listed in Table 2. We transformed the coordinates of the objects in the F350LP source list to carry out fixed-position PSF photometry in the F555W, F814W, and F160W master frames (no time-series measurements were obtained, only mean magnitudes). We performed an additional detection step on the F160W master frame after removing the stars that were present in the F350LP source list.

3. Cepheid Identification and Characterization

We applied the same Cepheid selection procedures as described by Y20 and identified 419 Cepheid candidates in NGC 4051. We measured their periods, amplitudes, and crowding bias corrections.

3.1. Cepheid Identification

Our Cepheid identification included four steps: variability index cut (Stetson 1996, adjusted for magnitude dependence), template fitting, period and amplitude cuts, and visual inspection. We first selected 4519 variable candidates with the Stetson index $L > 0.65$. This threshold was slightly higher than the initial choice for NGC 4151 ($L > 0.5$) for two reasons: (1) the minimum L value for NGC 4151 Cepheids that were eventually used for distance determination was $\sim$0.9; (2) the NGC 4051 field contains more Cepheid-yielding star-forming

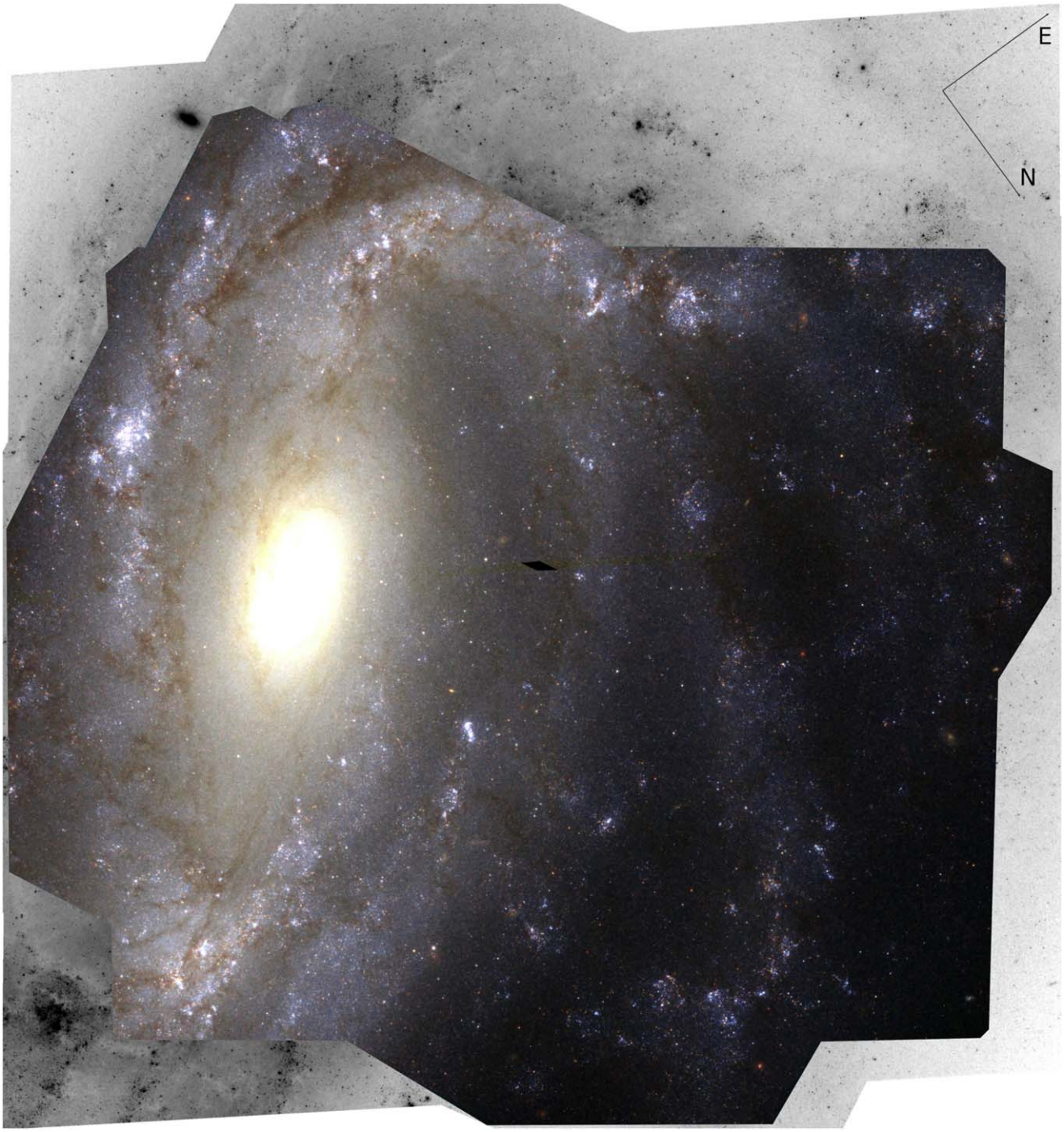

Figure 1. Pseudo-color image of NGC 4051 using our master frames in F350LP, F555W, F814W, and F160W as the luminance layer and the blue, green, and red channels, respectively. A square-root scaling was applied to all layers to increase the visibility. Color is only shown where all layers overlap, while an inverse gray scale is used in areas not imaged with F160W. The compass lines are 20″ in length. The black diamond-shaped area near the center is due to the gap between the Wide Field Camera 3/ultra-visible charge-coupled devices.

regions, and thus the number of variables is not a limiting factor for the NGC 4051 distance determination. Our goal is not to discover the complete set of Cepheids in NGC 4051 but rather to identify a high-purity sample that enables a precise and accurate distance determination. The L-magnitude distribution for NGC 4051 and our updated L threshold are shown in Figure 2. Second, we fit the Yoachim et al. (2009) Cepheid templates to the F350LP light curves of these variable candidates using the method described by Y20. Third, we restricted the sample based on the best-fit periods and amplitudes as done in Y20; this yielded 2804 objects with $P < 90$ d and peak-to-trough amplitudes between 0.4 and 1.7 mag. Finally, we visually inspected the phase-folded F350LP light curves of these 2804 objects and their overall matches to the best-fit Cepheid templates by overplotting measurements and templates. We identified 419 Cepheid candidates through this visual inspection process. Rejected objects are mostly non-variables with noisy measurements that passed our initial selection criteria. Light curves of all 2804 preselected objects are available as supplementary material.

Table 1
Observation Log

Epoch	MJD	Dither × Exposure Time (seconds)			
		F350LP	F555W	F814W	F160W
1	58089.2	3 × 350	⋯	⋯	2 × 553
2	58107.8	3 × 350	2 × 550	⋯	⋯
3	58111.9	3 × 350	⋯	2 × 550	⋯
4	58117.4	3 × 350	⋯	⋯	2 × 553
5	58122.6	3 × 350	2 × 550	⋯	⋯
6	58129.0	3 × 350	⋯	⋯	2 × 553
7	58135.6	3 × 350	⋯	2 × 550	⋯
8	58141.0	3 × 350	⋯	⋯	2 × 553
9	58145.3	3 × 350	2 × 550[a]	⋯	⋯
10	58149.6	3 × 350	⋯	⋯	2 × 553
11	58155.2	3 × 350	⋯	2 × 550	⋯
12	58162.1	3 × 350	⋯	⋯	2 × 553

Note.
[a] The first image of this set was excluded due to its poor FWHM, possibly due to increased jitter.

Table 2
Secondary Standards

R.A. [J2000]	Decl.	F350LP	F555W [mag(mmag)]	F814W
180.76803	44.53942	23.520(13)	23.604(18)	22.862(16)
180.77227	44.53125	23.943(15)	24.202(21)	23.034(14)
180.77507	44.52808	23.601(23)	23.707(19)	23.372(30)
180.77511	44.53187	23.566(17)	23.772(20)	22.798(20)
180.77630	44.53949	23.089(21)	23.228(20)	23.009(30)
180.77693	44.54960	23.822(19)	24.041(23)	22.981(21)
180.78067	44.54180	23.060(18)	23.309(23)	22.898(24)
180.78152	44.54246	22.434(11)	22.603(13)	21.713(11)
180.78185	44.51941	22.824(20)	22.894(15)	22.462(28)
180.78258	44.54943	23.771(18)	23.959(24)	23.325(31)

Note. Coordinates are based on the world coordinate system solution of the first F350LP image. Uncertainties are given in parentheses and are expressed in units of millimagnitude. This table is available in its entirety in machine-readable form.

(This table is available in its entirety in machine-readable form.)

Figure 3 shows 6 examples to illustrate the light-curve quality of the selected variables. The F350LP light the curves of all 419 visually selected objects are given in Table 3. Our motivation for this inspection is to obtain a high-purity sample, which is superior to a larger but possibly contaminated sample for distance measurement. Though subjective, visual inspection remains an effective and widely adopted method for the final Cepheid confirmation in extragalactic distance studies (e.g., Saha et al. 1996; Stetson et al. 1998; Fausnaugh et al. 2015; Hoffmann & Macri 2015; Hoffmann et al. 2016; Bentz et al. 2019).

Thanks to the template-fitting technique, Cepheid periods can be effectively recovered with sparsely sampled light curves. Typically, ∼12 epoch optical observations are designed to search for Cepheids in extragalactic systems and measure their periods (Madore & Freedman 1991). Because there are only four free parameters (including the period) in the model, it is relatively easy to recover the Cepheid periods with ∼12 measurements. However, we note that the light-curve sampling requires a span of ∼60–90 days and nonredundant spacings to ensure adequate phase coverage (Madore & Freedman 2005).

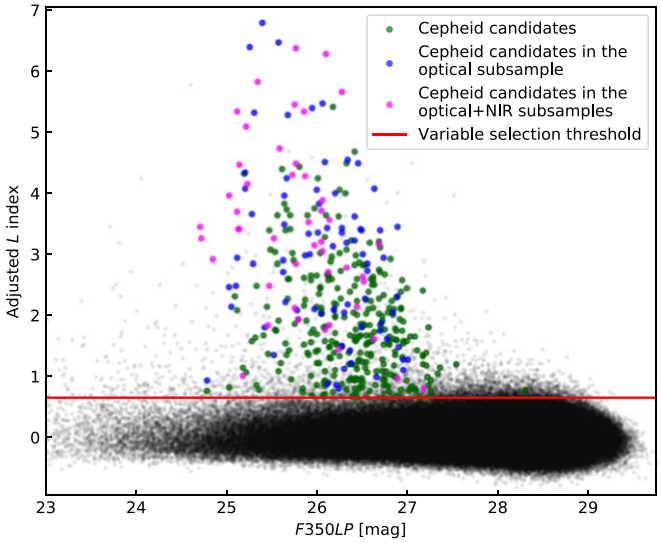

Figure 2. Adjusted L index against F350LP magnitudes for all the sources. The red line indicates our threshold for variable selection. Larger points indicate the 419 Cepheid candidates described in Section 3.1. The NIR subsample described in Section 4.1 is indicated by magenta points, while the optical subsample described in Section 4.1 is indicated by both magenta and blue points.

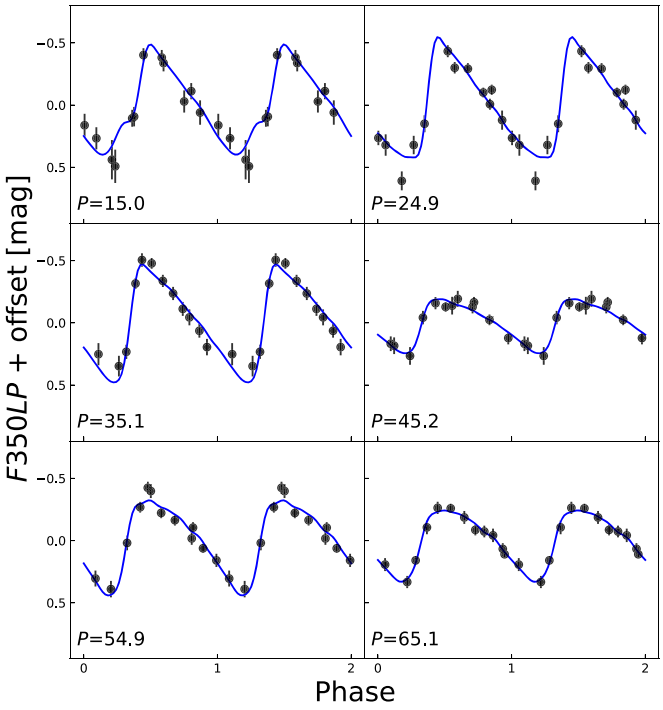

Figure 3. Example F350LP light curves of selected Cepheids spanning the period range. The blue curves indicate the best-fit Cepheid templates. We plot two cycles of pulsation for visualization purposes.

In this work, we solved the Cepheid periods using a nonlinear least-squares fitting method, with the exact methodology described in Y20. To ensure the global least-squares fit is reached, we included a grid of 150 logarithmically spaced initial trial periods from 10–120 days. We note that the fitting algorithm is allowed to converge to any period within the entire range, regardless of the starting trial value. As a result, for a given object, the 150 initial trial periods usually converged to only a few final values where χ^2 reached local minima. We

Table 3
F350LP Light Curves

Cepheid ID	t[a] [day]	mag [mag]	σ
9734	0.729	26.518	0.062
9734	19.282	26.473	0.070
9734	23.394	26.610	0.055
9734	28.883	26.705	0.079
9734	34.113	26.199	0.045
9734	40.468	26.267	0.067
9734	47.088	26.703	0.111
9734	52.458	26.353	0.053
9734	56.823	26.135	0.051
9734	61.067	26.201	0.051
9734	66.699	26.537	0.051
9734	73.602	26.595	0.078

Note.
[a] JD-2458089. This table is available in its entirety in machine-readable form.
(This table is available in its entirety in machine-readable form.)

adopted the output period with the lowest χ^2 as the best fit. For the 419 Cepheid candidates, we further estimated their period accuracy using the bootstrapping method. We computed the template-fitting residuals for each light curve, resampled and added them back to the original light curve, and then determined the residual-resampled light-curve period. This process was repeated 200 times, and the standard deviation of the resulting periods was adopted as the period uncertainty. We found a mean (median) relative period uncertainty $\Delta P/P$ of 2.0% (1.7%). The occurrences of $|\Delta P/P| > 0.05$ and 0.1 were 4% and 0.5%, respectively. Their contribution to the final distance error budget is studied in Section 4.2.

We considered whether the measurement uncertainty in period combined with the greater frequency of short period than long-period Cepheids could bias the period determination. Using a realistic distribution of periods we found for the mean case where $\sigma_{\log P} \sim 0.007$, the bias in the inferred period is about 2% of the period measurement uncertainty or $\Delta \log P = 0.00015$ and combined with the PLR a bias in the inferred magnitude of ~0.0004 mag. For Cepheids with periods closer to the span of the observations, $\log P \sim 1.8$, the mean bias rises to 5% of the uncertainty or $\Delta \log P = 0.00035$, and is still quite negligible. However, this bias can become important when the measurement uncertainty in $\log P$ exceeds 0.05 and the bias in the PLR approaches 0.01 mag.

3.2. Crowding Correction and Magnitude Calibration

We applied crowding, aperture, and phase corrections to the Cepheid magnitudes, then calibrated our photometric measurements on the Vega system.

While we adopted the same crowding correction method as for NGC 4151, we slightly updated our procedure in F160W relative to the method used in Y20. In our previous work, we only measured the F160W magnitude and crowding bias for Cepheids with $P > 25$ d. We removed such a restriction for this analysis; 379 of the optically discovered Cepheids were located in the smaller NIR field of view. Of these, 278 were detected and photometered. We determined their F160W crowding correction ΔF160W by carrying out three passes of the artificial star test procedure, compared to only one pass for NGC 4151. In the first pass, we determined the artificial star magnitudes using a PLR (with a slope fixed to −3.2 mag/dex) based on Cepheids with $P > 40$ d. In the next two passes, we based our calculation on Cepheids with $\sigma(\Delta\text{F160W}) < 0.25$ mag as determined from the preceding pass. The restriction of $P > 40$ d and $\sigma(\Delta\text{F160W}) < 0.25$ mag yielded a more accurate estimation of the input artificial star magnitudes, and our tests converged faster.

Unlike Y20, we derived aperture corrections using field stars (listed in Table 2) for F350LP, F555W, and F814W. In the case of F160W, we adopted the aperture correction value derived by Y20 due to the insufficient number of suitable stars in the respective master frame. All magnitudes presented in this paper are in the Vega system and were calibrated using the current STScI zero-points (see Section 4.2 of Y20 for the detailed method). The adopted Vega zero-points for "infinite aperture" magnitudes are 26.817, 25.843, 24.712, and 24.689 for F350LP, F555W, F814W, and F160W, respectively.

We present the Cepheid periods, amplitudes, fully calibrated magnitudes, and crowding corrections in Table 4. We adopted the Riess et al. (2019) PLR slopes of −2.76, −2.96, and −3.31 in F555W, F814W, and W^I (defined below), respectively. We iteratively fit these PLRs to our sample, rejecting the single largest $>3\sigma$ outlier in each step until convergence. We arrived at a final optically selected sample of 397 variables. Their color–magnitude diagram and optical PLRs are shown in Figures 4 and 5, respectively.

4. Results

We determined a distance to NGC 4051 of $D = 16.62 \pm 0.32$ Mpc, equivalent to a distance modulus of $\mu = 31.103 \pm 0.042$ mag, by applying the reddening-free Wesenheit indices (Madore 1982; Riess et al. 2019)

$$W^I = \text{F814W} - 1.3(\text{F555W} - \text{F814W}), \quad (1)$$

$$W^H = \text{F160W} - 0.386(\text{F555W} - \text{F814W}) \quad (2)$$

to Cepheid subsamples with precise measurements and averaging the W^I and W^H PLR offsets relative to the LMC. In this section, we present the details of this selection, the corresponding distance determination, and a comparison to results obtained with an alternative procedure (Riess et al. 2016).

4.1. Selection of Subsamples for Distance Determination

We selected high-quality subsamples of Cepheids for distance-determination purposes, in order to obtain tight Cepheid PLRs and reduce the noise from poorly measured outliers that were not detected in Section 3.2. The leading source of scatter in the W^I index is the uncertainty in the F555W crowding correction $\sigma(\Delta\text{F555W})$. Thus, we empirically determined a cut of $\sigma(\Delta\text{F555W}) < 0.1$ mag based on the weighted scatter of the W^I PLR residuals, as shown in the upper panel of Figure 6. We applied an iterative 3σ outlier rejection to obtain a subsample of 123 Cepheids for the optical distance determination. Similarly, we then applied a further empirical cut of $\sigma(\Delta\text{F160W}) < 0.3$ mag to arrive at a "NIR distance subsample" of 47 Cepheids, as shown in the lower panel of Figure 6. The weighted scatter of the full W^I and W^H samples are 0.35 and 0.41 mag, respectively, while the corresponding values for the distance-determination subsamples are 0.23 and 0.24 mag, respectively.

Table 4
Properties of Cepheid Candidates

ID	R.A. [J2000][a]	Decl.	P[b] [day]	L	Amp. [mag]	F350LP	F555W [mag (mmag)][c]	F814W	F160W	SB[d]	F[e]	ΔF555W	ΔF814W [mmag][f]	ΔF160W
82977	180.769100	44.538239	24.4(0.4)	1.69	0.938	26.236(103)	26.742(132)	25.362(150)	24.062(601)	308.0		−7(106)	3(120)	518(587)
88413	180.769205	44.537613	13.4(0.1)	2.27	1.157	26.617(133)	26.843(166)	26.142(239)	26.284(573)	295.3		57(145)	59(205)	1308(508)
142230	180.769992	44.531406	14.8(0.1)	3.63	0.885	26.257(158)	26.506(181)	25.572(184)	⋯	253.9		33(148)	−3(165)	⋯
129685	180.771219	44.533581	14.0(0.2)	0.86	0.479	26.440(113)	26.759(145)	25.610(178)	25.161(638)	251.5		13(127)	28(152)	926(614)
125827	180.771822	44.534374	76.8(7.1)	3.70	0.436	25.147(36)	25.584(69)	24.152(46)	22.963(222)	275.9	H	7(37)	9(36)	5(212)
115396	180.771970	44.535775	20.2(0.4)	0.71	0.830	26.049(171)	26.450(202)	25.146(292)	23.554(601)	304.2		67(156)	20(209)	692(592)
101787	180.772327	44.537594	58.6(2.2)	0.95	0.418	24.757(105)	25.149(93)	23.863(120)	22.090(288)	329.8	I	−13(66)	10(69)	48(275)
126388	180.772356	44.534583	11.0(0.1)	0.69	1.306	26.866(261)	27.180(311)	26.225(280)	⋯	284.8		11(272)	57(240)	⋯
42535	180.772570	44.545120	17.8(0.3)	1.60	1.124	26.847(129)	27.190(192)	25.969(188)	24.942(602)	283.4		38(140)	20(145)	836(578)
3059861	180.772803	44.541936	31.3(0.6)	1.92	0.873	25.746(225)	26.104(289)	25.114(181)	⋯	453.3		203(280)	133(153)	⋯
116297	180.772926	44.536114	19.9(0.5)	1.02	0.890	25.881(125)	26.134(148)	25.065(161)	24.084(505)	309.5		25(130)	−3(128)	704(484)
113897	180.772936	44.536426	16.0(0.3)	0.81	0.776	26.308(171)	26.774(217)	25.576(216)	25.216(530)	316.8		14(152)	10(173)	1172(504)
131049	180.772952	44.534324	46.7(1.0)	2.95	0.711	25.158(71)	25.398(92)	24.384(80)	24.125(427)	287.4	I	29(79)	23(67)	144(380)
153160	180.772990	44.531602	64.4(4.3)	3.01	0.728	25.693(61)	25.965(98)	24.992(83)	23.977(258)	263.3	o	8(60)	3(55)	−1(234)
38213	180.773388	44.546094	32.8(0.7)	3.74	0.812	25.618(118)	26.034(130)	24.824(121)	23.711(491)	280.3		20(121)	38(108)	315(485)
182138	180.773570	44.528351	26.3(0.7)	2.29	0.773	25.642(110)	25.953(142)	24.943(135)	24.022(457)	259.5		74(128)	42(116)	153(447)
49235	180.773713	44.544866	12.8(0.2)	0.87	0.711	26.690(211)	26.850(246)	25.791(277)	⋯	293.0		80(234)	46(254)	⋯
71671	180.774197	44.542297	49.0(0.9)	1.59	0.635	25.362(144)	25.635(173)	24.609(133)	⋯	430.9		114(159)	73(99)	⋯
81958	180.774332	44.541084	26.4(0.1)	1.48	0.994	26.225(185)	26.548(184)	25.664(174)	⋯	400.3		−6(147)	11(145)	⋯
201732	180.774472	44.526389	38.5(0.3)	1.95	0.888	25.739(104)	26.046(141)	24.944(113)	24.225(342)	239.1	H	−20(94)	−20(91)	44(276)

Notes.
[a] Coordinates from the first F350LP image.
[b] Period uncertainties are shown in the parentheses.
[c] Fully calibrated Vega-system magnitudes, including crowding corrections and their uncertainties.
[d] F160W-band local surface brightness in units of counts/s/sq arcsec.
[e] Cepheids used for W^I PLR (I), for both W^I and W^H PLRs (H), or rejected from optical PLRs (o).
[f] Crowding corrections and uncertainties. This table is available in its entirety in machine-readable form.

(This table is available in its entirety in machine-readable form.)

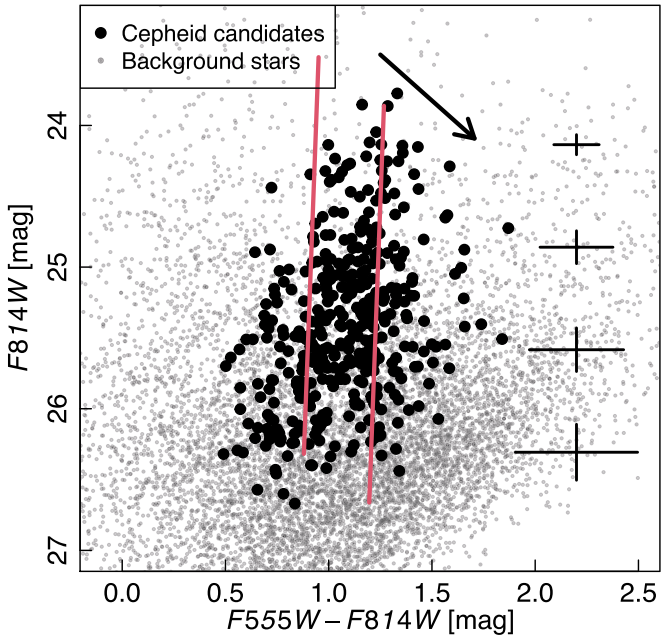

Figure 4. Color–magnitude diagram of optically selected Cepheids (filled symbols). Representative error bars are shown on the right. Gray dots are a subsample of field stars. The area between the red lines shows the Cepheid instability strip for $P > 10$ d, derived from Large Magellanic Cloud (LMC) observations (Riess et al. 2019). The arrow indicates the effect of $A_V = 1$ mag.

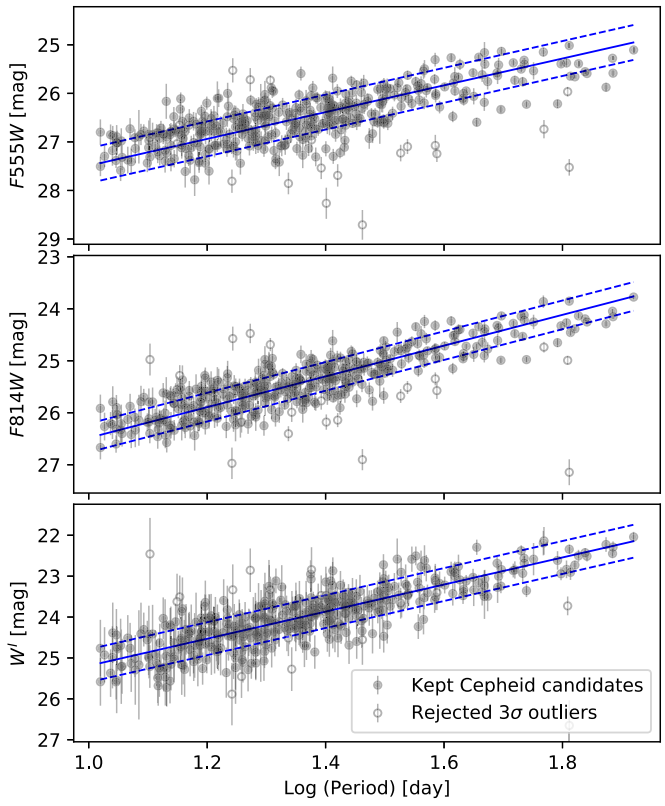

Figure 5. F555W (top), F814W (middle), and W^I (bottom) PLRs for optically selected Cepheids (filled circles). Rejected variables are indicated by open circles. The blue solid and dashed lines indicate the best-fit PLRs and $\pm$ 1σ scatter, respectively.

These selection criteria are different from those adopted by Y20, where we applied cuts on period and F160W surface brightness. Indeed, the crowding correction uncertainty is

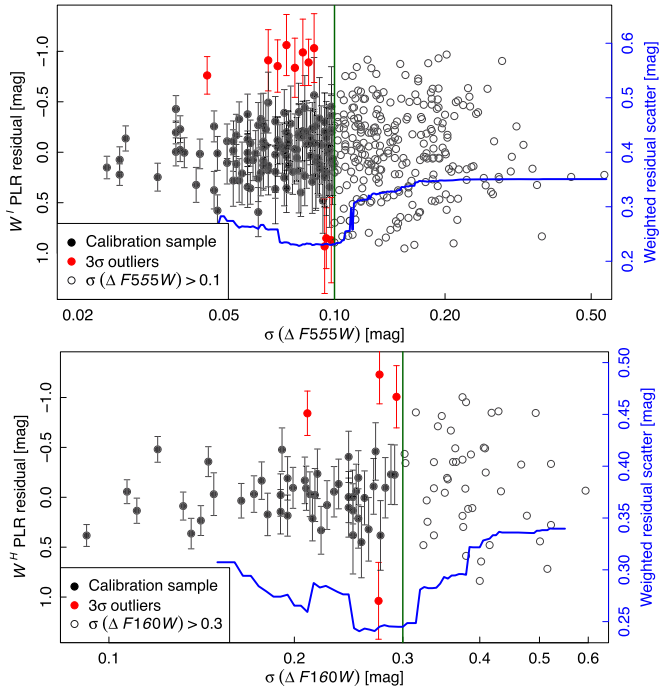

Figure 6. Optical (upper) and NIR (lower) subsamples used for distance determination, selected through limits on crowding correction uncertainty and iterative 3σ outlier rejection. The selected Cepheids, rejected outliers, and excluded Cepheids are indicated by black filled circles, red filled circles, and gray open circles, respectively. The blue curves show the weighted scatter of PLR residuals as a function of maximum crowding correction uncertainty, while the green vertical lines indicate our adopted cuts.

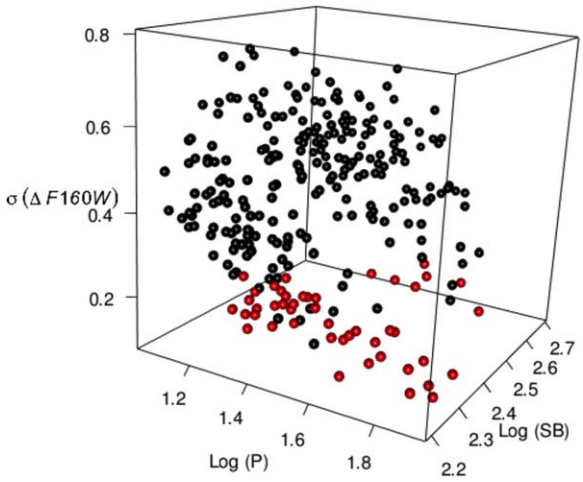

Figure 7. 3-D plot showing the correlation between the pairs among σ (ΔF160W), period, and local surface brightness (SB). The NIR subsample used for distance determination is indicated by red points. An interactive version of this plot that allows rotation and zoom is available in the online article.

strongly correlated with period (or luminosity) and local surface brightness, as shown in Figure 7. We had noted in Section 4.3 of Y20 that a cut on $\sigma(\Delta$F160W) yielded results consistent with those obtained via a cut on local surface brightness. Figure 8 shows the positions of all Cepheids, color coded by subsample. We expect that a long-period or low-crowding Cepheid subsample will be minimally impacted by systematics.

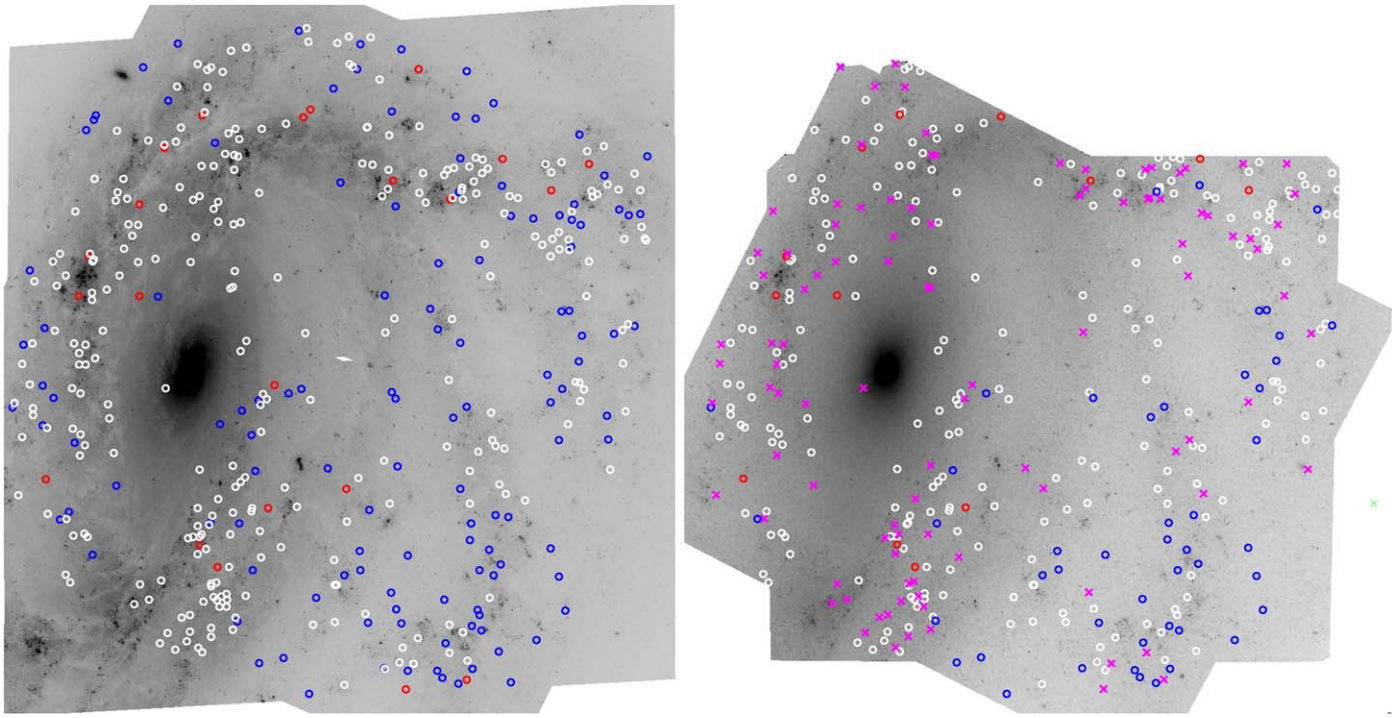

Figure 8. Optical (left) and NIR (right) grayscale images of NGC 4051 showing the locations of Cepheids from various subsamples. Blue, white, and red circles denote Cepheids used for distance determination, excluded variables, and rejected objects, respectively (matching the black, red, and open symbols used in Figure 6). Magenta crosses in the right panel indicate optically selected Cepheids that were not detected in the NIR frame.

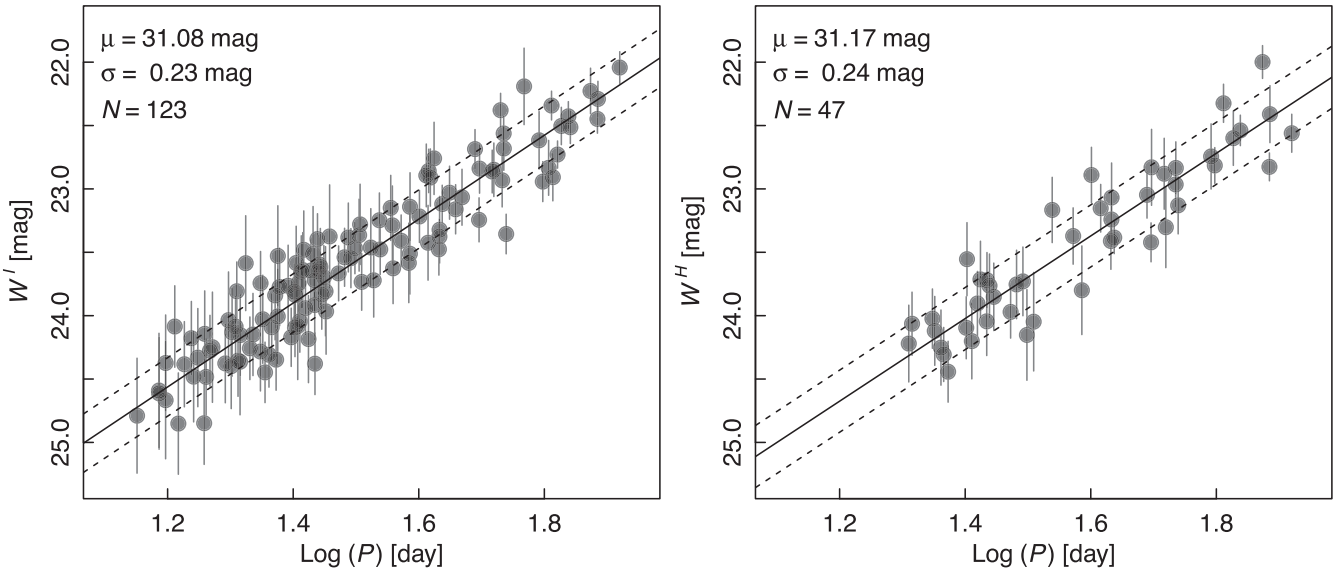

Figure 9. Optical (left) and NIR (right) Wesenheit PLRs for the Cepheid subsamples used for distance determination. The solid lines indicate the best-fit PLRs, while the dashed lines indicate the 1σ standard deviations.

4.2. The Distance to NGC 4051

We present the optical and NIR reddening-free Wesenheit PLRs for the distance-determination Cepheid subsamples in Figure 9. The PLR fit results are summarized in Table 5. The LMC-relative distance moduli are based on the Cepheid PLRs reported by Riess et al. (2019) and include a correction of + 0.021 mag to our F160W photometry to account for the difference in the adopted Vega-based zero-point. The W^I and W^H PLRs yielded $\Delta\mu_I = 12.602 \pm 0.041$ and $\Delta\mu_H = 12.672 \pm 0.057$ mag, respectively. These two measurements are consistent within 1σ, and their combination yields $\Delta\mu = 12.626 \pm 0.033$ mag. We note that the combined uncertainty of 0.033 mag can be slightly underestimated as W^H and W^I and are partially correlated due to the color term in W^H. However, the F160W term is independent of W^I and contributes 2.6× more than the color term. Thus, we conclude that taking the weighted mean of the W^I- and W^H-based distances is a reasonable approximation. Madore & Freedman (1991), Groenewegen & Oudmaijer (2000), and Inno et al. (2013) suggested similar approaches that average distances from PLRs of different

Table 5
Wesenheit PLRs used for Distance Determination

Index	Expression		Slope	Intercept		Weighted Scatter	N
				LMC	N 4051		
W^I	$F814W - 1.3$	$(F555W - F814W)$	−3.31	15.933	28.535	0.23	123
W^H	$F160W - 0.386$	$(F555W - F814W)$	−3.26	15.915[a]	28.587[b]	0.24	47

Notes.
[a] Corrected for the F160W-band count-rate nonlinearity; see Y20 for details.
[b] Adjusted by 0.021 mag for the difference in adopted Vega zero-points between Riess et al. (2019) and this study.

Table 6
Error Budget

Source	W^I (mag)		W^H (mag)
PLR scatter	0.021		0.035
PLR slope	...		0.033
Magnitude calibration	0.01		0.02
Metallicity	0.03		0.02
Phase correction	0.009		0.004
Reddening law	0.01		...
Period error	0.006		0.01
Subtotal	0.041		0.057
Subtotal combined		0.033	
LMC distance		0.026	
Total	0.048		0.062
Total combined		0.042	

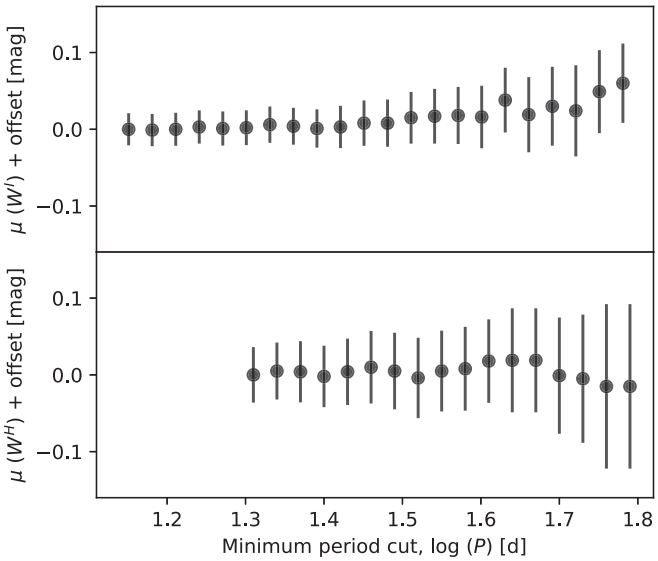

Figure 10. Distance dependence on minimum period cut for the optical (upper) and NIR (lower) Cepheid subsamples.

wavelengths. We adopt the LMC distance modulus of $\mu_{\rm LMC} = 18.477 \pm 0.026$ mag (Pietrzyński et al. 2019) to arrive at a distance modulus for NGC 4051 of $\mu = 31.103 \pm 0.042$ mag, equivalent to a distance of $D = 16.62 \pm 0.32$ Mpc.

We present our error budget in Table 6 using the same format as that used for NGC 4151 by Y20, with the addition of an error term from Cepheid period uncertainties. We derived the latter with Monte Carlo simulations. We randomly drew periods from Gaussian distributions whose standard deviations are determined with bootstrapping (see Section 3.1), then fit PLR to these simulations 1000 times. We found the resulting distance modulus errors due to period uncertainty are 0.006 and 0.010 mag for W^I and W^H, respectively. Compared to our earlier work, we adopted a smaller and conservative magnitude calibration error of 0.01 mag for the optical PLR because we derived the F814W and F555W aperture corrections using field stars. The phase correction errors were also reduced as a result of the increased number of Cepheids in NGC 4051. The other entries are identical to NGC 4151. We estimated the uncertainty due to possible metallicity effects by using the [O/H] dispersion in 21 Cepheid hosts and the terms reported by Riess et al. (2016). We refer interested readers to Section 4.4 of Y20 for a detailed discussion of those systematics. We did not find a distance dependence on the minimum period cut for either the optical or NIR Cepheid subsamples, as shown in Figure 10.

We compared our distance determination to literature values, as compiled by the NASA/IPAC Extragalactic Database (NED). While the uncertainties in most of those previous determinations are too large to provide a statistically meaningful comparison against our result, Yoshii et al. (2014) derived a distance with comparable precision as ours. They used the AGN time-lag method and dust reverberation modeling to obtain a distance of $D = 17.6 \pm 0.6$ Mpc. Their result is consistent with ours within 1.4σ, though we note that their distance determination for NGC 4151 is not consistent with ours, as reported by Y20.

4.3. Comparison to the Supernovae, H0, for the Equation of State (SH0ES) Procedure

The SH0ES project (Riess et al. 2016) measures Cepheid F160W magnitudes following a different procedure, which gives us an opportunity to compare the two photometry approaches. We carried out SH0ES photometry on the NGC 4051 F160W master image and derived NIR PLRs for a sample of Cepheids that were selected using the SH0ES criteria. Both methods use fixed-position PSF photometry in F160W, with positions derived from the higher signal-to-noise ratio and better-sampled optical master frame. Likewise, they both use artificial star tests to correct for crowding. Unlike this study, where we fixed positions for all sources appearing in both the F350LP and F160W images, the SH0ES approach only fixes the positions for the Cepheids.

In addition, the SH0ES procedure includes two features to derive accurate photometry and Gaussian errors in magnitude space, as demonstrated in artificial star tests (see the bottom panel of Figure 11): (1) a large "protection" radius of $0.75\times$ FWHM to avoid spurious de-blends; (2) the selection of artificial stars that match the apparent source displacement of

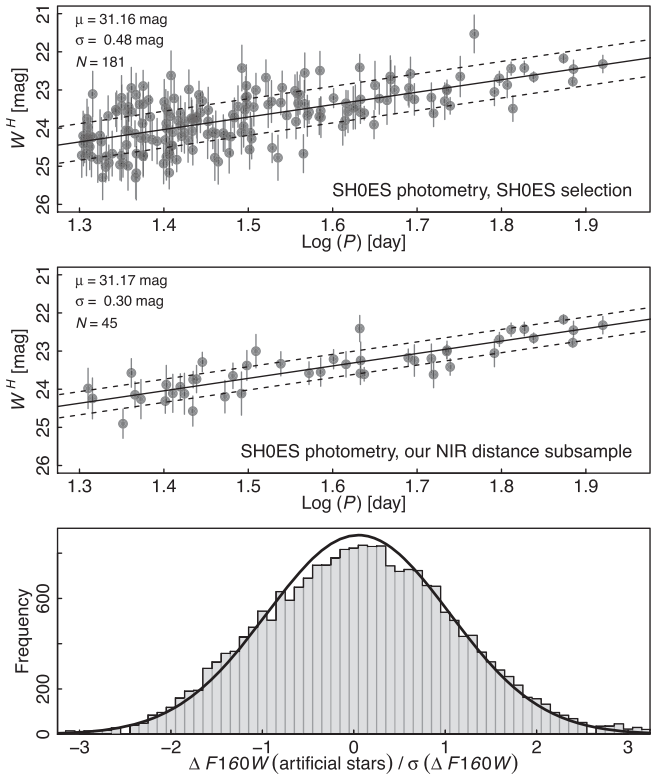

Figure 11. Top panel: NIR Cepheid PLRs using SH0ES F160W photometry and SH0ES selection criteria. The resultant distance modulus and weighted PLR scatter are shown in the top-left of the panel. Middle panel: same as the top but for our NIR calibration sample. Bottom panel: error distribution of the SH0ES artificial star tests. For each artificial star, we subtracted the mean bias correction and divided by the standard deviation of all artificial stars associated with the same Cepheid.

the Cepheid relative to the predicted optical position (a secondary consequence of blending, Riess et al. 2009). As a result, the SH0ES approach yielded unbiased photometry for a broader range of local crowding levels and thus resulted in a larger sample of Cepheids for distance determination. As shown in the top panel of Figure 11, the SH0ES criteria yielded 182 Cepheids and a distance modulus of 31.16 mag using the same aforementioned PLR slope. We also determined a distance modulus using the SH0ES-based photometry for 45 Cepheids that are in common with our NIR subsample, which yielded 31.17 mag (middle panel of Figure 11). Both are in excellent agreement (to within 0.01 mag) with our results. We expect a statistical uncertainty between methods mostly due to the finite number of unique samples of artificial stars, ∼0.006 mag, and a systematic uncertainty arising from the choice of different PSFs, sky background regions, fitting techniques, etc., ∼0.02 mag.

This comparison is only a cross-check of the F160W photometry and the NIR subsample selection between the SH0ES approach and the methods adopted in this work. We refer interested readers to Javanmardi et al. (2021) for a comprehensive and fully independent comparison of all steps in the SH0ES methodology.

5. Discussion

Our Cepheid-based distance to NGC 4051 is close to the high end of the literature values, which range from ∼9 to 18 Mpc and are mostly based on the Tully & Fisher (1977)

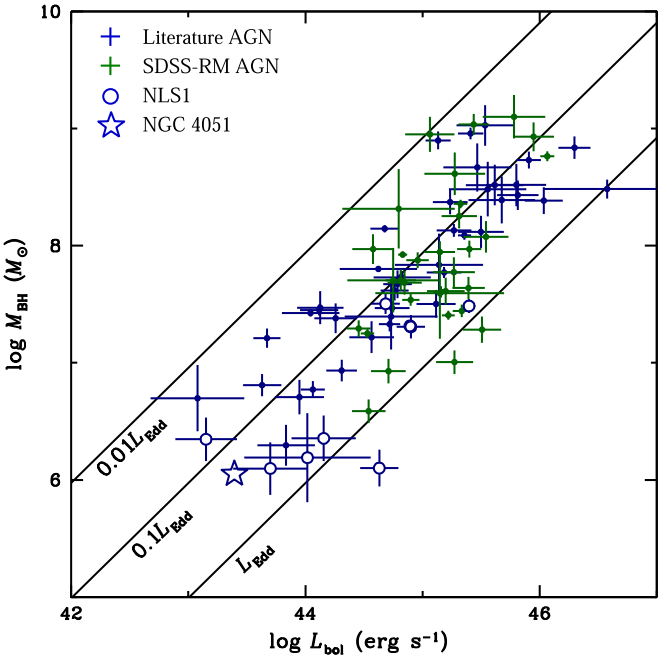

Figure 12. Black hole mass vs. bolometric luminosity for AGNs with reverberation-based masses using the Hβ emission line. Shown in blue are sources gathered from the literature by Dalla Bontà et al. (2020, their Table A1); shown in green are Sloan Digital Sky Survey (SDSS)-RM AGNs with Hβ-based reverberation masses (Grier et al. 2017) as compiled by Dalla Bontà et al. (2020, their Table A2). NLS1s are shown as open circles. The updated measurement for NGC 4051 is represented by the open star in the lower left of the diagram.

relationship. The bright central AGN in NGC 4051 is generally not accounted for in Tully–Fisher studies, thus biasing the studies that use blue imaging toward smaller distances (Robinson et al., submitted). Additionally, NGC 4051 may have increased star formation, when compared to comparable quiescent galaxies, as has been found for many active galaxies in the local universe (Xue et al. 2010). An elevated star formation rate may lead to an elevated surface brightness (e.g., Graves & Faber 2010; Mould 2020), which would also serve to bias Tully–Fisher distances toward smaller values. Finally, NGC 4051 has a lower inclination than is generally recommended for Tully–Fisher studies and thus increases the uncertainty in the resultant distance (Kourkchi et al. 2020). We discuss the implications of the Cepheid-based distance in Sections 5.1 and 5.2, and the NGC 4051 galactic motion in Section 5.3.

5.1. Eddington Ratio in NGC 4051

Peterson et al. (2004) and Collin et al. (2006) recognized that there might be a problem with the redshift-based distance to NGC 4051, and it was these concerns that led us to this investigation. Peterson et al. (2004, their Figure 16) and Collin et al. (2006, their Figure 6) showed that the Eddington ratio in NGC 4051 was surprisingly low for an NLS1 galaxy, one of only two such objects with $\dot{m} < 0.1$ (the other is MCG-06-30-15; Bentz et al. 2016). Now, at the corrected distance of 16.6 Mpc, the Eddington ratio is $\dot{m} \approx 0.2$, a value more typical of NLS1 galaxies. In Figure 12, we update the mass–luminosity diagram of Peterson et al. (2004), where we see that the improved and increased distance places NGC 4051 in the same

locus as other NLS1s, with $\dot{m} \gtrsim 0.1$, instead of the seemingly odd value implied by previous distance estimates.

5.2. Revisiting the Energetics of the Nucleus

It seems that the most commonly assumed distance for NGC 4051 is the redshift-based distance of 9.3 Mpc, which is considerably smaller than the value reported here. This has a significant effect on linear distances within the galaxy, which now become a factor of 1.8 larger, and luminosity measures, which increase by a factor of 3.2.

Barbosa et al. (2009), for example, estimated the mass outflow rate and power along with three other Seyfert galaxies. Repeating their outflow calculation and increasing the diameter of the eastern outflow from 45–80 pc results in an outflow rate $\dot{M} = 2.2\, n_{100} f\, M_{\odot}\ \mathrm{yr}^{-1}$, where n_{100} is the electron density in units of $100\ \mathrm{cm}^{-3}$ and f is the volume filling factor, for which Barbosa et al. (2009) suggest a value of 10^{-3}. We similarly correct the diameter of the western outflow from 44.5–79.2 pc, thus increasing the outflow rate to $1.4\, n_{100} f M_{\odot}\ \mathrm{yr}^{-1}$. The total outflow rate is the sum of these, $\dot{M} = 3.6\, n_{100} f\ M_{\odot}\ \mathrm{yr}^{-1}$. Similarly, recalculation of the kinetic luminosity gives

$$P = \frac{1}{2}\dot{M}V^2 = 2.6 \times 10^{40} n_{100} f\ \mathrm{erg\ s}^{-1}, \quad (3)$$

where V is the outflow velocity.

Barbosa et al. (2009) compared the mass outflow rate to the mass accretion rate required to sustain the luminosity, but unfortunately using a bolometric luminosity that was much too low. The luminosity they use traces back to a Chandra X-ray observation obtained in 2000 April, when NGC 4051 was in an extremely faint X-ray state (Collinge et al. 2001); NGC 4051 has some history of the X-rays nearly turning off for long periods of time (Uttley et al. 1999; Peterson et al. 2000). We instead use the bolometric luminosity from Dalla Bontà et al. (2020), which adjusted to our distance of 16.6 Mpc becomes $\log L_{\mathrm{bol}} = 43.38$. It is worth noting at this point that the kinetic luminosity of the outflow is some six orders of magnitude less than the radiative luminosity for $f \sim 10^{-3}$.

The corrected mass accretion rate is thus

$$\dot{M}_{\mathrm{acc}} = \frac{L_{\mathrm{bol}}}{\eta\, c^2} = 0.0042\, M_{\odot}\ \mathrm{yr}^{-1}, \quad (4)$$

where we have taken the efficiency to have the nominal value $\eta = 0.1$. Barbosa et al. (2009) argued that if the total outflow rate exceeds the accretion rate, then the outflow must be comprised of accelerated circumnuclear material. In our revised calculation, this condition is met if $f \gtrsim 10^{-3} n_{100}^{-1}$.

On the other hand, the analysis of high-velocity outflows in NGC 4051 by Pounds (2014) does not need reassessment as a distance of 15.2 Mpc, based on a Tully–Fisher measurement, was assumed (Pounds & Vaughan 2011a, 2011b; Pounds & King 2013). Adjustment to a distance of 16.6 Mpc results in little change.

5.3. Galactic Motion

NGC 4051 is a member of what is often referred to as the Ursa Major Cluster (Tully et al. 1996). *CosmicFlows-3* (Tully et al. 2016) reports an overall distance to Ursa Major of 17.2 ± 1.0 Mpc, which agrees with our Cepheid distance to NGC 4051 within the quoted uncertainty. Over the years, it has become clear that the Ursa Major complex is likely composed of several distinct bound groups (Karachentsev et al. 2013; Kourkchi & Tully 2017). Both Karachentsev et al. (2013) and Kourkchi & Tully (2017) place NGC 4051 into a group with the lenticular galaxy NGC 4111 as the brightest member. Kourkchi & Tully (2017) list 14 members in the group, and have redshift-independent distances for five of these galaxies. With this information, they derive a weighted average *group* distance of 14.36 ± 1.01 Mpc, which is broadly consistent with our derived Cepheid distance to NGC 4051 when taking into account the size of the group itself.

The observed velocity of NGC 4051 in the reference frame of the Local Group is $v_{\mathrm{LG}} = 740 \pm 3\ \mathrm{km\ s}^{-1}$ (Karachentsev & Makarov 1996). Adopting a value of the Hubble constant of $74.0 \pm 1.4\ \mathrm{km\ s}^{-1}\ \mathrm{Mpc}^{-1}$ (Riess et al. 2019) allows us to calculate a peculiar velocity of $v_{\mathrm{pec}} = -490 \pm 34\ \mathrm{km\ s}^{-1}$. While seemingly high, we note that the vast majority of galaxies in the Ursa Majoris complex exhibit a negative peculiar velocity, with an average peculiar velocity with respect to the Local Group of $v_{\mathrm{pec}} = -337\ \mathrm{km\ s}^{-1}$ (Karachentsev et al. 2013). Similarly, Pak et al. (2014) identified 166 Ursa Major members and found that they lie in a redshift range of 620–1208 $\mathrm{km\ s}^{-1}$. Considering that all these galaxies are roughly equidistant, the peculiar velocity of NGC 4051 lies well within the inferred peculiar velocity range of other Ursa Major galaxies. When placed in this context, our derived distance to NGC 4051 is consistent with expectations.

6. Summary

We analyzed HST time-series observations for the Seyfert 1 galaxy NGC 4051 and identified 419 Cepheid candidates in this system. Using subsamples of Cepheids that were precisely measured at optical and NIR wavelengths, we derived a distance of $D = 16.6 \pm 0.3$ Mpc, equivalent to a distance modulus of $\mu = 31.10 \pm 0.04$ mag. We calculated the Eddington ratio of the AGN residing in this galaxy to be $\dot{m} \approx 0.2$, thus confirming NGC 4051 as a typical NLS1 in terms of the AGN mass–luminosity ratio. We obtained a peculiar velocity of $-490 \pm 34\ \mathrm{km\ s}^{-1}$ for NGC 4051 and compared it to those of the other Ursa Major member galaxies. We revisited the energetics of the NGC 4051 nucleus based on Barbosa et al. (2009) and derived an outflow rate of $\sim 3.6 \times 10^{-3}\, M_{\odot}\ \mathrm{yr}^{-1}$ and an outflow kinetic luminosity of $\sim 2.6 \times 10^{37}\ \mathrm{erg\ s}^{-1}$ if $n_{100} f \sim 10^{-3}$ was assumed, as well as a mass accretion rate of $\sim 4.2 \times 10^{-3}\, M_{\odot}\ \mathrm{yr}^{-1}$.

We thank K.Z. Stanek for helpful advice early in this project, and the anonymous referee for providing valuable comments. M.M.F. and B.M.P. thank Tod Lauer for an enlightening conversation. Support for HST program GO-13765 was provided by NASA through a grant from the Space Telescope Science Institute, which is operated by the Association of Universities for Research in Astronomy, Inc., under NASA contract NAS5-26555. M.C.B. gratefully acknowledges support from the NSF through grant No. AST-2009230. M.V. gratefully acknowledges support from the Independent Research Fund Denmark via grant No. DFF 8021-00130. This research has made use of the NASA/IPAC Extragalactic Database (NED), which is funded by the National Aeronautics and Space Administration and operated by the California Institute of Technology.

Appendix
Supplementary Material

We include light curves (in electronic form) for 2804 objects that passed our initial cuts (prior to visual selection). Light curves are shown in the same form as one of the panels of Figure 3. The file names are in the format of `<id>.pdf` where `<id>` is our internal tracking identifier. The figures are compressed and grouped into two tarballs, selected.tar.gz and `rejected.tar.gz`, based on our visual inspection results.

ORCID iDs

W. Yuan https://orcid.org/0000-0001-9420-6525
L. M. Macri https://orcid.org/0000-0002-1775-4859
B. M. Peterson https://orcid.org/0000-0001-6481-5397
A. G. Riess https://orcid.org/0000-0002-6124-1196
M. M. Fausnaugh https://orcid.org/0000-0002-9113-7162
S. L. Hoffmann https://orcid.org/0000-0002-4312-7015
G. S. Anand https://orcid.org/0000-0002-5259-2314
M. C. Bentz https://orcid.org/0000-0002-2816-5398
E. Dalla Bontà https://orcid.org/0000-0001-9931-8681
R. I. Davies https://orcid.org/0000-0003-4949-7217
G. De Rosa https://orcid.org/0000-0003-3242-7052
L. Ferrarese https://orcid.org/0000-0002-8224-1128
C. J. Grier https://orcid.org/0000-0001-9920-6057
E. K. S. Hicks https://orcid.org/0000-0002-4457-5733
C. A. Onken https://orcid.org/0000-0003-0017-349X
R. W. Pogge https://orcid.org/0000-0003-1435-3053
T. Storchi-Bergmann https://orcid.org/0000-0003-1772-0023
M. Vestergaard https://orcid.org/0000-0001-9191-9837

References

Barbosa, F. K. B., Storchi-Bergmann, T., Cid Fernandes, R., Winge, C., & Schmitt, H. 2009, MNRAS, 396, 2
Bentz, M. C., Cackett, E. M., Crenshaw, D. M., et al. 2016, ApJ, 830, 136
Bentz, M. C., Ferrarese, L., Onken, C. A., Peterson, B. M., & Valluri, M. 2019, ApJ, 885, 161
Collin, S., Kawaguchi, T., Peterson, B. M., & Vestergaard, M. 2006, A&A, 456, 75
Collinge, M. J., Brandt, W. N., Kaspi, S., et al. 2001, ApJ, 557, 2
Dalla Bontà, E., Peterson, B. M., Bentz, M. C., et al. 2020, ApJ, 903, 112
Davies, R. I., Maciejewski, W., Hicks, E. K. S., et al. 2014, ApJ, 792, 101
Fausnaugh, M. M., Kochanek, C. S., Gerke, J. R., et al. 2015, MNRAS, 450, 3597
Fischer, T. C., Crenshaw, D. M., Kraemer, S. B., & Schmitt, H. R. 2013, ApJS, 209, 1
García-Burillo, S., & Combes, F. 2012, JPhCS, 372, 012050
Graves, G. J., & Faber, S. M. 2010, ApJ, 717, 803
Grier, C. J., Trump, J. R., Shen, Y., et al. 2017, ApJ, 851, 21
Groenewegen, M. A. T., & Oudmaijer, R. D. 2000, A&A, 356, 849
Hicks, E. K. S., Davies, R. I., Maciejewski, W., et al. 2013, ApJ, 768, 107
Hoffmann, S. L., & Macri, L. M. 2015, AJ, 149, 183
Hoffmann, S. L., Macri, L. M., Riess, A. G., et al. 2016, ApJ, 830, 10
Hopkins, P. F., & Quataert, E. 2010, MNRAS, 405, L41
Inno, L., Matsunaga, N., Bono, G., et al. 2013, ApJ, 764, 84
Javanmardi, B., Mérand, A., Kervella, P., et al. 2021, ApJ, 911, 12
Karachentsev, I. D., & Makarov, D. A. 1996, AJ, 111, 794
Karachentsev, I. D., Nasonova, O. G., & Courtois, H. M. 2013, MNRAS, 429, 2264
Kocevski, D. D., Faber, S. M., Mozena, M., et al. 2012, ApJ, 744, 148
Kourkchi, E., & Tully, R. B. 2017, ApJ, 843, 16
Kourkchi, E., Tully, R. B., Eftekharzadeh, S., et al. 2020, ApJ, 902, 145
Leavitt, H. S., & Pickering, E. C. 1912, HarCi, 173, 1
Madore, B. F. 1982, ApJ, 253, 575
Madore, B. F., & Freedman, W. L. 1991, PASP, 103, 933
Madore, B. F., & Freedman, W. L. 2005, ApJ, 630, 1054
Mould, J. 2020, FrASS, 7, 21
Osterbrock, D. E., & Pogge, R. W. 1985, ApJ, 297, 166
Pak, M., Rey, S.-C., Lisker, T., et al. 2014, MNRAS, 445, 630
Peterson, B. M., Ferrarese, L., Gilbert, K. M., et al. 2004, ApJ, 613, 682
Peterson, B. M., McHardy, I. M., Wilkes, B. J., et al. 2000, ApJ, 542, 161
Pietrzyński, G., Graczyk, D., Gallenne, A., et al. 2019, Natur, 567, 200
Pounds, K. 2014, SSRv, 183, 339
Pounds, K. A., & King, A. R. 2013, MNRAS, 433, 1369
Pounds, K. A., & Vaughan, S. 2011a, MNRAS, 413, 1251
Pounds, K. A., & Vaughan, S. 2011b, MNRAS, 415, 2379
Riess, A. G., Casertano, S., Yuan, W., Macri, L. M., & Scolnic, D. 2019, ApJ, 876, 85
Riess, A. G., Macri, L., Casertano, S., et al. 2009, ApJ, 699, 539
Riess, A. G., Macri, L. M., Hoffmann, S. L., et al. 2016, ApJ, 826, 56
Riffel, R. A., Storchi-Bergmann, T., Winge, C., et al. 2008, MNRAS, 385, 1129
Riffel, R. A., Storchi-Bergmann, T., & Winge, C. 2013, MNRAS, 430, 2249
Saha, A., Sandage, A., Labhardt, L., et al. 1996, ApJ, 466, 55
Schawinski, K., Simmons, B. D., Urry, C. M., Treister, E., & Glikman, E. 2012, MNRAS, 425, L61
Schnorr-Müller, A., Storchi-Bergmann, T., Nagar, N. M., & Ferrari, F. 2014, MNRAS, 438, 3322
Seyfert, C. K. 1943, ApJ, 97, 28
Simões Lopes, R. D., Storchi-Bergmann, T., de Fátima Saraiva, M., & Martini, P. 2007, ApJ, 655, 718
Sorce, J. G., Tully, R. B., Courtois, H. M., et al. 2014, MNRAS, 444, 527
Stetson, P. B. 1987, PASP, 99, 191
Stetson, P. B. 1994, PASP, 106, 250
Stetson, P. B. 1996, PASP, 108, 851
Stetson, P. B., Saha, A., Ferrarese, L., et al. 1998, ApJ, 508, 491
Storchi-Bergmann, T., & Schnorr-Müller, A. 2019, NatAs, 3, 48
Tully, R. B., Courtois, H. M., & Sorce, J. G. 2016, AJ, 152, 50
Tully, R. B., & Fisher, J. R. 1977, A&A, 500, 105
Tully, R. B., Verheijen, M. A. W., Pierce, M. J., Huang, J.-S., & Wainscoat, R. J. 1996, AJ, 112, 2471
Uttley, P., McHardy, I. M., Papadakis, I. E., Guainazzi, M., & Fruscione, A. 1999, MNRAS, 307, L6
Wang, J.-M., Du, P., Hu, C., et al. 2014, ApJ, 793, 108
Xue, Y. Q., Brandt, W. N., Luo, B., et al. 2010, ApJ, 720, 368
Yoachim, P., McCommas, L. P., Dalcanton, J. J., & Williams, B. F. 2009, AJ, 137, 4697
Yoshii, Y., Kobayashi, Y., Minezaki, T., Koshida, S., & Peterson, B. A. 2014, ApJL, 784, L11
Yuan, W., Fausnaugh, M. M., Hoffmann, S. L., et al. 2020, ApJ, 902, 26